An Improved Global Land Anthropogenic Aerosol Product Based on Satellite Retrievals From 2008 to 2016

Chen Liang, Zhou Zang, Zhanqing Li[ID], and Xing Yan[ID]

Abstract—**Significant levels of aerosols originate from anthropogenic activities, markedly influencing regional air quality and, consequently, human health. Generally, fine-mode aerosol optical depth (fAOD) data are used to evaluate the concentration of anthropogenic aerosols. Although the moderate resolution imaging spectroradiometer (MODIS) provides fine-mode fraction (FMF) data that can be used to produce fAOD products, these data remain highly uncertain over land, in terms of global validation, relative to Aerosol Robotic Network (AERONET) measurements. To overcome this limitation, we developed an improved global land-scale fAOD product combining the lookup table-spectral deconvolution algorithm (LUT-SDA), generalized additive model (GAM), and MODIS Collection 6.1 aerosol products. Validation of the improved product revealed that over 63% of the fAOD values are within an expected error (EE) envelope of $\pm(0.05 + 15\%)$, with strong positive correlations ($R^2 = 0.65$) and low bias (root-mean-square error = 0.185; mean absolute error = 0.104) compared to AERONET-observed fAOD values. Furthermore, the fAOD developed eliminates the multiple zeroes in the MODIS FMF-based fAODs. In the improved fAOD product, eastern China and northern India exhibit the highest 9-year-mean fAOD loading, with values generally exceeding 0.6. The improved global land fAOD product provides a new avenue with which to obtain data on anthropogenic aerosols and can also be useful in aerosol–climate interaction research.**

Index Terms—**Anthropogenic aerosols, fine-mode aerosol optical depth (fAOD), lookup table-spectral deconvolution algorithm (LUT-SDA), moderate resolution imaging spectroradiometer (MODIS).**

I. INTRODUCTION

AEROSOLS commonly contain fine particles that significantly impact the climate system and human health [1], [2]. Many climate modeling studies in recent decades reveal that aerosols probably have a critical effect on

Chen Liang, Zhou Zang, and Xing Yan are with the State Key Laboratory of Remote Sensing Science, College of Global Change and Earth System Science, Beijing Normal University, Beijing 100875, China (e-mail: yanxing@bnu.edu.cn).

Zhanqing Li is with the Earth System Science Interdisciplinary Center, Department of Atmospheric and Oceanic Science, University of Maryland, College Park, MD 20742 USA.

monsoonal precipitation [3]–[5], convective precipitation [6], solar radiation [7]–[9], and tropical cyclones [10], [11]. Considering various effects of aerosols mentioned, obtaining accurate aerosol data and the spatiotemporal characteristics is crucial.

Lee and Chung [12] stated that the fine-mode aerosol optical depth (fAOD) is useful for inferring the concentration of anthropogenic aerosols. Although there have been some regional-scale studies on fAOD in recent years [8], [13], [14], global-scale studies of fAOD remain limited. Local fAOD data can be achieved by means of *in situ* observation; however, the scarcity of global fAOD data is accentuated by the lack of experimental data with adequate spatiotemporal resolution. Currently, the two main ways of obtaining fAOD data involve retrieval from satellite images and ground-based measurements. Although the ground-based measurements like the Aerosol Robotic Network (AERONET) guarantee the accuracy of the fAOD data, measurement sites are sparse and the data commonly lack a spatial view. Consequently, many studies are conducted based on satellite remote sensing data because these involve global-scanning coverage and higher spatial resolutions [12].

In recent years, satellites including the moderate resolution imaging spectroradiometer (MODIS), the multiangle imaging spectroradiometer (MISR), and Himawari-8 released official data on aerosol properties [15]–[17]. MODIS data, which come from the Terra and Aqua spacecraft, provide numerous global aerosol products on a daily, weekly, or even monthly basis [18], [19]. It is the most popular source of AOD information [18]–[20]. Kaufman *et al.* [21] used MODIS over-ocean AOD measurements and the fine-mode fraction (FMF) to evaluate the anthropogenic optical thickness over the oceans and reported that the anthropogenic aerosol radiative forcing is about -1.4 ± 0.4 W/m^2. Kleideman *et al.* [22] compared MODIS and AERONET retrieval of over-ocean aerosol FMFs and found that MODIS slightly overestimated the FMFs for dust-dominated aerosols. The most current MODIS AOD product is Collection 6.1 (C6.1). This collection has already been validated at the scale of global, regional, and individual sites and proved to have a high accuracy over land [23], [24]. However, despite the high accuracy of MODIS AOD products, MODIS fAOD remains highly uncertain over land [19]. An important parameter for satellite-based fAOD calculation is the FMF, which represents the fine-mode aerosol fraction of the total AOD, i.e., FMF = fAOD/AOD. However, some studies indicate that the land FMF retrieved from the MODIS

is not credible [12], [19], [20], and thereby complicating the use of MODIS fAOD products. Jethva *et al.* [14] compared the MODIS fAOD and FMF with those from AERONET at Kanpur, northern India, and reported an underestimation and many zero values among most matched cases. In addition, Lee and Chung [12] compared global fAOD products from MODIS and MISR with AERONET observations, with the results revealing a low bias in fAODs from MODIS and MISR compared to AERONET. Yan *et al.* [25] also demonstrated that MODIS C6 underestimated the FMF in most areas of Asia, involving many zero values. Thus, the MODIS FMF product remains limited and unable to provide accurate global fine aerosol levels and spatial distribution characteristics.

In response, this research aims to develop an improved global land fAOD product using 2008–2016 MODIS C6.1 satellite data, here termed *Ensemble fAOD*. This letter is a continuation of our previous research [25], [26]. The fAOD product will be validated by data from global AERONET sites. A comprehensive comparison with MODIS FMF-based fAOD will further highlight the utility of the product proposed in this study.

II. DATA SETS AND METHODS

A. MODIS Data

The over-land MODIS AOD data used in this study are from the MODIS C6.1 level-3 daily (MOD08_D3) product from 2008 to 2016, with a $1° \times 1°$ horizontal resolution, and was acquired by the MODIS sensor aboard the National Aeronautics and Space Administration (NASA)-Electrical Optical Systems Inc. (EOS) Terra spacecraft. The three AOD data sets in the product include dark target (DT)-, deep blue (DB)-, and DT–DB merged-based (DTDB)-AOD. The latest C6.1 DT-AOD data were updated through a second-generation operational DT algorithm developed by Levy *et al.* [19]. The latest DB data set was produced by the enhanced DB algorithm [27], providing only the over-land product. The combined DT and DB aerosol data set has the advantages of both the DT and DB algorithms and the normalized difference vegetation index (NDVI) was used to merge the data sets [19]. The merged data set expanded the spatial coverage over land mainly because of the improvements in the DT algorithm over significantly dark regions of low vegetation [19]. The names used for the MODIS data sets are "AOD_Land_Mean," "DB_AOD_550_Land_Mean," and "AOD_550_DT&DB_Combined_Mean"; these correspond to the DT, DB, and DTDB data sets, respectively. In addition, all three data sets are AOD values at 550-nm band.

B. AERONET AOD Data

The AERONET is a global ground-based aerosol observation network; it provides multiwavelength AOD from direct solar radiation measurements, characterized by high accuracy and an uncertainty of 0.01–0.02 [28] and are used as "ground truth" data for satellite product validation [20]. This study used AERONET version 2 L2.0 (cloud screened and quality assured) AOD data product from 2008 to 2016. The study area and the locations of the 171 AERONET sites

chosen for this study are shown in Supplementary Fig. S1. The selected AERONET sites had continuous observation data for the nine years investigated. The AERONET fAOD observations were recorded within ±30 min of the MODIS overpass. However, MODIS fAODs are associated with the 550-nm wavelength while AERONET measurements only provide fAODs at 500 nm. Consequently, to compare fAODs at the same wavelength, the AERONET 500-nm fAODs were interpolated to 550 nm using their Ångström exponent (AE) ("AE-Fine_Mode_500nm [α_f]").

C. FMF Data and fAOD Retrievals From MODIS

As the global-scale FMF was removed from the C6 MOD08 product [19], we obtained the MODIS global FMF from NASA's Earth Observations data (https://neo.sci.gsfc.nasa.gov/), which are based on the Collection 5 aerosol algorithm [15] (processing for the data set ended on October 7, 2016). The MODIS FMF product over land is produced only by the DT method.

Yan *et al.* [26] proposed an improved FMF retrieval method termed the lookup table-spectral deconvolution algorithm (LUT-SDA) using two wavelengths of MODIS-derived AOD and AE data. A 4D LUT was created based on the SDA method [29] to describe the relationship between the AEs of the AOD and fAOD, the AE derivative, and FMF. Yan *et al.* [25] updated the LUT-SDA for FMF retrieval by considering seasonal AOD characteristics and validated it over Asia. In this letter, we used MODIS C6.1 MOD08_D3 AODs at wavelengths of 470 and 660 nm and employed the LUT-SDA algorithm such as Yan *et al.* [25] to calculate FMFs at 550 nm. Then, we extended it to a global scale and denoted it LUT-SDA FMF.

The fAOD was then calculated according to Lee and Chung [12] as follows:

$$\text{fAOD} = \text{FMF} \times \text{AOD} \tag{1}$$

with the AOD data obtained from MODIS C6.1 MOD08_D3 AOD products. According to (1), we applied the MODIS C5 FMF and LUT-SDA FMF for the global over-land fAOD retrievals. The derived fAOD products are called MODIS FMF-based fAOD and LUT-SDA FMF-based fAOD, respectively.

D. Improved Global fAOD Ensemble Product

We clustered the study domain into nine regions (Supplementary Fig. S2) based on Sayer *et al.* [24]. We then used a generalized additive model (GAM) to generate a new fAOD ensemble in each region. The GAM is a nonparametric model in which the dependent variables depend linearly on the smooth functions of the predictors [30]. The Ensemble fAOD is expressed as

$$\text{fAOD}_{i,j} = \alpha_{j,r} + s_i\left(\text{DT}_{i,j}\right) + s_i\left(\text{DB}_{i,j}\right) \\ + s_i\left(\text{DTDB}_{i,j}\right) + e_{i,j}; \quad e_{i,j} \sim N\left(0, \sigma_{j,r}^2\right) \tag{2}$$

where $\text{fAOD}_{i,j}$ represents the ensemble fAOD values at $i = 1 \sim i_r$ grid cells in each of the 16 geographical regions indexed

by r on day j; $\alpha_{j,r}$ is a daily intercept representing the mean across all grid cells in region r, $s_i()$ is a smooth function of the corresponding parameter for the ith location, $e_{i,j}$ is an error that can be determined by $N(0, \sigma_{j,r}^2)$, and $DT_{i,j}$, $DB_{i,j}$, and $DTDB_{i,j}$ are the LUT-SDA FMF-based fAOD products on day j in grid cell i. A schematic describing the Ensemble fAOD calculation is shown in Supplementary Fig. S3.

E. Validation Methods

We referred to some statistical metrics to assess the quality, performance, and uncertainty of fAOD retrievals, including the Pearson's linear correlation coefficient (R), root-mean-square error (RMSE), mean absolute error (MAE), and expected error {EE = [±(0.05 + 15%)] [19]}. When the MODIS AOD falls within the EE envelope, it is considered accurate. The R, RMSE, and MAE calculation formula are shown as follows (3)–(5), as shown at the bottom of this page.

In these formulas, $fAOD_i$ refers to MODIS FMF-based fAOD or Ensemble fAOD and $fAOD_{(AERO)_i}$ refers to AERONET fAOD measurements at the ith AERONET site.

III. RESULTS

A. Spatial Characteristics of the MODIS-FMF-Based fAOD and the Developed fAOD Ensemble

The spatial characteristics of the nine-year (2008–2016) means from the MODIS FMF-based fAOD are displayed in Fig. 1(a), where the spatial distribution is based on only those pixels having daily fAOD samples of over 80 days per year. These data were retrieved from the MODIS C5 FMF and MODIS C6.1 DTDB AOD products. The over-land MODIS FMF product is produced by the DT algorithm, and the MODIS AOD product used here is based on the DT and DB algorithms. We showed a MODIS FMF-based DTDB fAOD product here due to its high accuracy and good performance in most regions; detailed information regarding data selection is provided in Supplementary Section S1. The MODIS FMF-based fAOD high-value regions (with values > 0.4) in Fig. 1(a) are primarily in the Amazon region and Laos. The MODIS FMF-based fAODs display highest values, those exceeding 0.6, over Laos. The low-value regions are mainly on the west coast of the USA and in Europe, Australia, the Middle East, and North Africa, with values generally below 0.1. We thoroughly verified the LUT-SDA FMF-based fAOD product as shown in Supplementary Section S2. We found that the LUT-SDA FMF-based DTDB fAODs exhibited the best
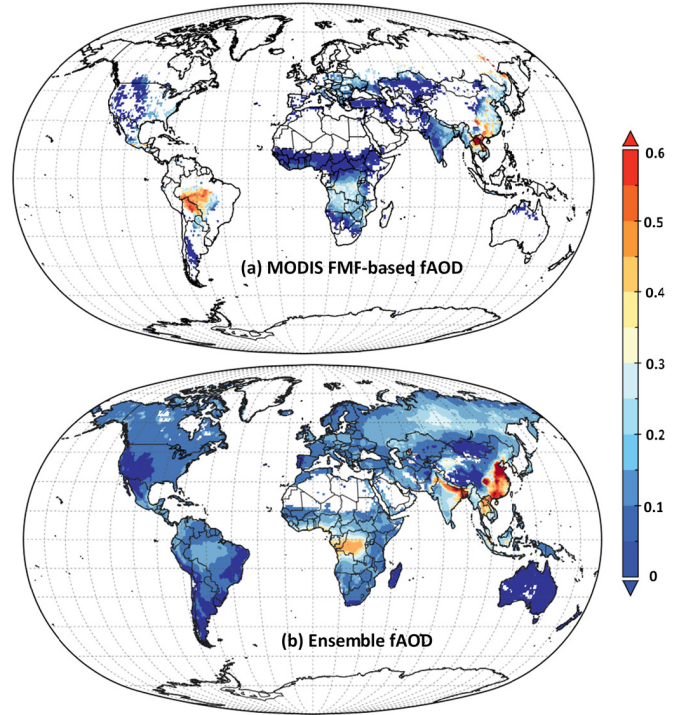

Fig. 1. Global spatial distribution of mean values for (a) MODIS FMF-based fAODs and (b) Ensemble fAODs from 2008 to 2016 (the spatial distribution is based on only those pixels having daily fAOD samples of over 80 days per year).

performance. However, its performance in Asia was worse than the performance of LUT-SDA FMF-based DB fAOD; it is therefore unsatisfactory for that reason. Therefore, by directly adopting the LUT-SDA FMF-based DTDB fAOD product, the spatial accuracy in Asia will worsen despite the overall performance of the DTDB fAOD being the best. Thus, based on the method detailed in Section II-D, we developed a new fAOD product termed Ensemble fAOD which showed an overall improvement based on the LUT-SDA FMF-based fAODs.

The mean spatial distribution of the Ensemble fAOD product from 2008 to 2016 is shown in Fig. 1(b), where the spatial distribution is based on only those pixels having daily fAOD samples of over 80 days per year. The high-value regions are concentrated in eastern China, north India, and central Africa. The highest-value region is in eastern China, exceeding 0.6 in the Beijing–Tianjin–Hebei region. In addition, two other high-value regions are present in the southwest and south China. Conversely, the low-value areas are on the west coast of the

$$R = \frac{\sum_{i=1}^{n} (fAOD_i - \overline{fAOD})(fAOD_{(AERO)_i} - \overline{fAOD_{(AERO)}})}{\sqrt{\sum_{i=1}^{n} (fAOD_i - \overline{fAOD})^2} \sqrt{\sum_{i=1}^{n} (fAOD_{(AERO)_i} - \overline{fAOD_{AERO}})^2}} \tag{3}$$

$$RMSE = \sqrt{\frac{1}{n} \sum_{i=1}^{n} (fAOD_i - fAOD_{(AERO)_i})^2} \tag{4}$$

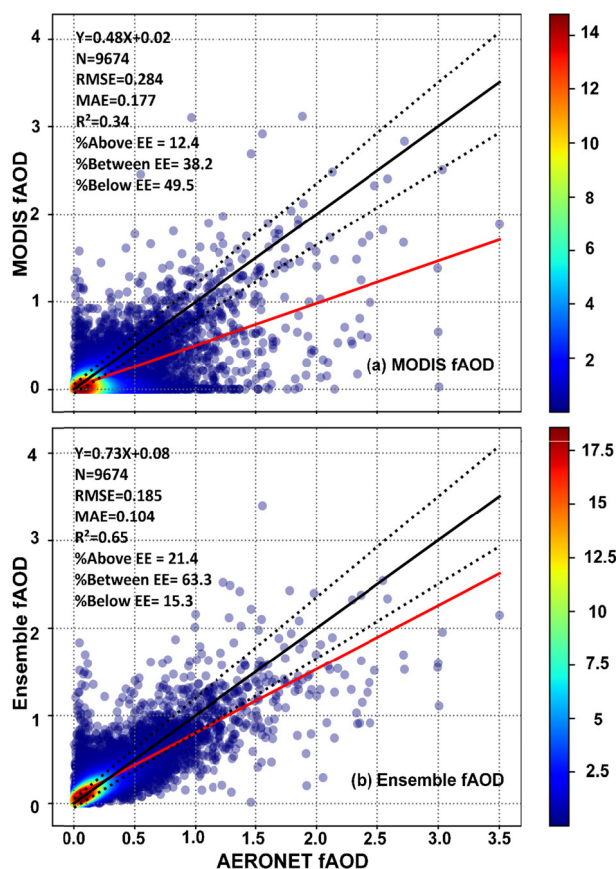$$MAE = \frac{1}{n} \sum_{i=1}^{n} |fAOD_i - fAOD_{(AERO)_i}| \tag{5}$$

Fig. 2. Density scatterplots of (a) MODIS fAOD and (b) Ensemble fAOD against AERONET fAOD from 2008 to 2016 for 171 AERONET sites. The solid and dotted lines are, respectively, the 1:1 line and the EE for fAOD $\pm(0.05 + 15\%)$.

USA and in Europe, Australia, the Middle East, and southern South America, with fAOD values of about 0.1 and below. The distribution characteristics of Ensemble fAOD are quite different from those based on the MODIS FMF. In the Amazon region, the fAOD values in the Ensemble fAOD range from about 0.1 to 0.3, whereas in the MODIS FMF-based fAODs, these vary from 0.5 to 0.6.

B. Validation of the New Global Ensemble fAOD

This study collected nine-year AERONET data ($N = 9674$) at 171 global sites for validation. A comparison of the overall validation between the MODIS FMF-based fAOD products and the Ensemble fAOD for 2008–2016 is depicted in Fig. 2. By contrast, the square of the correlation coefficient (R^2) for the Ensemble fAOD is 0.65 while that for the MODIS FMF-based fAOD is 0.34, indicating an improvement of nearly 0.3 associated with the Ensemble fAOD. The RMSE (0.185) and MAE (0.104) values of the Ensemble fAOD are also significantly lower than those of the MODIS DB fAOD (RMSE of 0.284 and MAE of 0.177). Approximately 63.3% of the Ensemble fAOD values are within the EE and the improved values in Fig. 2 show that the Ensemble fAOD overcomes the incidence of zero or close-to-zero values in the MODIS fAOD. A comparison of the spatial improvement between the Ensemble fAOD and the MODIS FMF-based fAOD is shown in Supplementary Fig. S4. Noticeably, most

sites around the world show improved data based on the Ensemble fAOD compared data based on the MODIS FMF, especially in Asia, where the RMSEs decreased by 0.05 and the fraction within the EE increased by 10%–15% averagely. Detailed information on the evaluation of the Ensemble fAOD for the 171 AERONET sites for 2008–2016 is presented in Supplementary Table S1.

IV. DISCUSSION

Kaufman et al. [2] presented a global distribution of fAODs derived from MODIS measurements and confirmed the distribution using aerosol model results. The data presented in Kaufman et al. [2] from MODIS measurements and aerosol models revealed fAODs above 0.45 mainly in the south and east Asia, central South America, and central Africa. Myhre [31] used global aerosol model and combined ground-based measurement and satellite observations to produce two AOD distributions. The high fAOD loadings in these areas are attributed to human activity including fossil fuel and biomass combustion [32]. The Ensemble fAOD developed in this study displays the highest values, generally above 0.5, in eastern China; this is consistent with these studies [2], [31]. Che et al. [8] measured AOD in situ over eastern China and reported AOD values of 0.68–0.76 at urban and rural sites with an FMF value of about 0.9. Therefore, we infer fAODs of about 0.6 over eastern China, which is also consistent with our Ensemble fAOD results. In addition, two additional high-value areas in Ensemble fAOD are in southwestern and southern China. One example is the Sichuan Basin. Because of the lower topography of the basin and its relatively humid climate, aerosols there with strong hygroscopicity can easily form regional pollution and do not spread much [33]. The Ensemble fAOD values in the Amazon region, which reach 0.3, are attributed to frequent forest fires in the Amazon region. It is estimated that about 20% of biomass burning originates from wildfires [34]. As such appearances of fine organic particle occurrences are mainly caused by natural sources that are less hygroscopic than regional pollution aerosols, their fAOD values are lower than those from anthropogenic sources. This is consistent with the conclusion of Kaufman et al. [2].

The Ensemble fAOD was derived from satellite data based on the LUT-SDA and GAM, rather than from simulations like in Lee and Chung [12], Chung et al. [7], and Myhre [31]; therefore, daily real-time fAODs were obtainable. As illustrated in Jiang et al. [4], anthropogenic aerosols affect radiation budgets and changes in the spatial distribution of AODs. The distribution of AODs and the shortwave flux changes exhibited, induced by anthropogenic aerosols, likely resemble the distribution of the Ensemble fAODs, with the higher value regions concentrated in eastern China and northern India. Therefore, the Ensemble fAOD has higher accuracy than the MODIS-derived fAODs and provides more accurate information as a global over-land fAOD product. This would be useful for future research on radiation balance, monsoonal precipitation, and tropical storms related to anthropogenic aerosols. Moreover, the Ensemble fAOD seems to be an effective auxiliary tool for estimating ambient fine particle matter such as the surface $PM_{2.5}$ concentrations [26].

V. CONCLUSION

In this letter, a new global-scale fAOD over-land product termed Ensemble fAOD was developed and validated. The Ensemble fAOD overcame limitations exhibited by the MODIS FMF-based fAODs including high uncertainties in magnitude and many zero values. The Ensemble fAOD displayed high-value regions mainly in eastern China, north India, and central Africa, with values generally above 0.4. The fAOD value was the highest in eastern China, especially in the Beijing–Tianjin–Hebei region where it exceeded 0.6. Based on the nine-year data of 9674 colocations at 171 AERONET over-land sites worldwide, validation of the Ensemble fAOD revealed $>63\%$ of the fAOD values were within the EE envelope of $\pm(0.05 + 15\%)$, with high correlation ($R^2 = 0.65$) and low bias (RMSE $= 0.185$; MAE $= 0.104$). Regarding the improved accuracy compared to the MODIS FMF-based fAODs, the Ensemble fAOD reduced the RMSE by almost 0.1, MAE by 0.073, and increased the values within the EE by 25.1% and R^2 by 0.31.

REFERENCES

[1] C. A. Pope III, M. Ezzati, and D. W. Dockery, "Fine-particulate air pollution and life expectancy in the United States," *New England J. Med.*, vol. 360, no. 4, pp. 376–386, 2009.

[2] Y. J. Kaufman, D. Tanré, and O. Boucher, "A satellite view of aerosols in the climate system," *Nature*, vol. 419, no. 6903, pp. 215–223, Sep. 2002.

[3] M. A. Bollasina, Y. Ming, and V. Ramaswamy, "Anthropogenic aerosols and the weakening of the South Asian summer monsoon," *Science*, vol. 334, no. 6055, pp. 502–505, Oct. 2011.

[4] Y. Jiang, X. Liu, X.-Q. Yang, and M. Wang, "A numerical study of the effect of different aerosol types on east asian summer clouds and precipitation," *Atmos. Environ.*, vol. 70, pp. 51–63, May 2013.

[5] D. Polson, M. Bollasina, G. C. Hegerl, and L. J. Wilcox, "Decreased monsoon precipitation in the Northern Hemisphere due to anthropogenic aerosols," *Geophys. Res. Lett.*, vol. 41, no. 16, pp. 6023–6029, Aug. 2014.

[6] S. Yu *et al.*, "Anthropogenic aerosols are a potential cause for migration of the summer monsoon rain belt in China," *Proc. Nat. Acad. Sci. USA*, vol. 113, no. 16, pp. E2209–E2210, Apr. 2016.

[7] C. E. Chung *et al.*, "Global fine-mode aerosol radiative effect, as constrained by comprehensive observations," *Atmos. Chem. Phys.*, vol. 16, no. 13, pp. 8071–8080, 2016.

[8] H. Che *et al.*, "Aerosol optical properties and direct radiative forcing based on measurements from the China Aerosol Remote Sensing Network (CARSNET) in eastern China," *Atmos. Chem. Phys.*, vol. 18, no. 1, pp. 405–425, 2018.

[9] F. Paulot, D. Paynter, P. Ginoux, V. Naik, and L. W. Horowitz, "Changes in the aerosol direct radiative forcing from 2001 to 2015: Observational constraints and regional mechanisms," *Atmos. Chem. Phys.*, vol. 18, no. 17, pp. 13265–13281, 2018.

[10] Y. Wang, K.-H. Lee, Y. Lin, M. Levy, and R. Zhang, "Distinct effects of anthropogenic aerosols on tropical cyclones," *Nature Climate Change*, vol. 4, no. 5, pp. 368–373, May 2014.

[11] N. J. Dunstone, D. M. Smith, B. B. B. Booth, L. Hermanson, and R. Eade, "Anthropogenic aerosol forcing of Atlantic tropical storms," *Nature Geosci.*, vol. 6, no. 7, pp. 534–539, Jul. 2013.

[12] K. Lee and C. E. Chung, "Observationally-constrained estimates of global fine-mode AOD," *Atmos. Chem. Phys.*, vol. 13, no. 5, pp. 2907–2921, 2013.

[13] B. Mai *et al.*, "Column-integrated aerosol optical properties of coarse- and fine-mode particles over the Pearl River Delta region in China," *Sci. Total Environ.*, vols. 622–623, pp. 481–492, May 2018.

[14] H. Jethva, S. K. Satheesh, J. Srinivasan, and R. C. Levy, "Improved retrieval of aerosol size-resolved properties from Moderate Resolution Imaging Spectroradiometer over India: Role of aerosol model and surface reflectance," *J. Geophys. Res.*, vol. 115, no. D18, pp. 1–10, 2010.

[15] R. C. Levy, L. A. Remer, S. Mattoo, E. F. Vermote, and Y. J. Kaufman, "Second-generation operational algorithm: Retrieval of aerosol properties over land from inversion of Moderate Resolution Imaging Spectroradiometer spectral reflectance," *J. Geophys. Res., Atmos.*, vol. 112, no. D13, pp. 1–21, Jul. 2007.

[16] D. J. Diner *et al.*, "The value of multiangle measurements for retrieving structurally and radiatively consistent properties of clouds, aerosols, and surfaces," *Remote Sens. Environ.*, vol. 97, no. 4, pp. 495–518, Sep. 2005.

[17] M. Kikuchi, H. Murakami, K. Suzuki, T. M. Nagao, and A. Higurashi, "Improved hourly estimates of aerosol optical thickness using spatiotemporal variability derived from Himawari-8 geostationary satellite," *IEEE Trans. Geosci. Remote Sens.*, vol. 56, no. 6, pp. 3442–3455, Jun. 2018.

[18] L. A. Remer *et al.*, "The MODIS aerosol algorithm, products, and validation," *J. Atmos. Sci.*, vol. 62, no. 4, pp. 947–973, 2005.

[19] R. C. Levy *et al.*, "The Collection 6 MODIS aerosol products over land and ocean," *Atmos. Meas. Techn.*, vol. 6, no. 11, pp. 2989–3034, 2016.

[20] R. C. Levy *et al.*, "Global evaluation of the Collection 5 MODIS dark-target aerosol products over land," *Atmos. Chem. Phys.*, vol. 10, no. 21, pp. 10399–10420, 2010.

[21] Y. J. Kaufman, O. Boucher, D. Tanré, M. Chin, L. A. Remer, and T. Takemura, "Aerosol anthropogenic component estimated from satellite data," *Geophys. Res. Lett.*, vol. 32, no. 17, pp. 1–4, Sep. 2005.

[22] R. G. Kleidman *et al.*, "Comparison of Moderate Resolution Imaging Spectroradiometer (MODIS) and Aerosol Robotic Network (AERONET) remote-sensing retrievals of aerosol fine mode fraction over ocean," *J. Geophys. Res.*, vol. 110, no. D22, pp. 1–6, 2005.

[23] Y. Wang, Q. Yuan, T. Li, H. Shen, L. Zheng, and L. Zhang, "Evaluation and comparison of MODIS Collection 6.1 aerosol optical depth against AERONET over regions in China with multifarious underlying surfaces," *Atmos. Environ.*, vol. 200, pp. 280–301, Mar. 2019.

[24] A. M. Sayer, N. C. Hsu, J. Lee, W. V. Kim, and S. T. Dutcher, "Validation, stability, and consistency of MODIS Collection 6.1 and VIIRS Version 1 Deep Blue aerosol data over land," *J. Geophys. Res., Atmos.*, vol. 124, no. 8, pp. 4658–4688, Apr. 2019.

[25] X. Yan *et al.*, "An improved algorithm for retrieving the fine-mode fraction of aerosol optical thickness—Part 2: Application and validation in Asia," *Remote Sens. Environ.*, vol. 222, pp. 90–103, Mar. 2019.

[26] X. Yan, Z. Li, W. Shi, N. Luo, T. Wu, and W. Zhao, "An improved algorithm for retrieving the fine-mode fraction of aerosol optical thickness, part 1: Algorithm development," *Remote Sens. Environ.*, vol. 192, pp. 87–97, Apr. 2017.

[27] N. C. Hsu *et al.*, "Enhanced Deep Blue aerosol retrieval algorithm: The second generation," *J. Geophys. Res., Atmos.*, vol. 118, no. 16, pp. 9296–9315, Aug. 2013.

[28] B. N. Holben *et al.*, "An emerging ground-based aerosol climatology: Aerosol optical depth from AERONET," *J. Geophys. Res., Atmos.*, vol. 106, no. D11, pp. 12067–12097, Jun. 2001.

[29] N. T. O'Neill, T. F. Eck, A. Smirnov, B. N. Holben, and S. Thulasiraman, "Spectral discrimination of coarse and fine mode optical depth," *J. Geophys. Res.*, vol. 108, no. D17, pp. 1–15, 2003.

[30] Q. Xiao, H. H. Chang, G. Geng, and Y. Liu, "An ensemble machine-learning model to predict historical PM$_{2.5}$ concentrations in China from satellite data," *Environ. Sci. Technol.*, vol. 52, no. 22, pp. 13260–13269, Nov. 2018.

[31] G. Myhre, "Consistency between satellite-derived and modeled estimates of the direct aerosol effect," *Science*, vol. 325, no. 5937, pp. 187–190, Jul. 2009.

[32] T. F. Eck *et al.*, "Climatological aspects of the optical properties of fine/coarse mode aerosol mixtures," *J. Geophys. Res.*, vol. 115, no. D19, pp. 1–20, 2010.

[33] G. Ning *et al.*, "Characteristics of air pollution in different zones of Sichuan Basin, China," *Sci. Total Environ.*, vol. 612, pp. 975–984, Jan. 2018.

[34] P. V. Hobbs, J. S. Reid, R. A. Kotchenruther, R. J. Ferek, and R. Weiss, "Direct radiative forcing by smoke from biomass burning," *Science*, vol. 275, no. 5307, pp. 1777–1778, Mar. 1997.

Supporting Information for

An improved global land anthropogenic aerosol product

based on satellite retrievals from 2008-2016

Chen Liang, Zhou Zang, Zhanqing Li, Xing Yan*
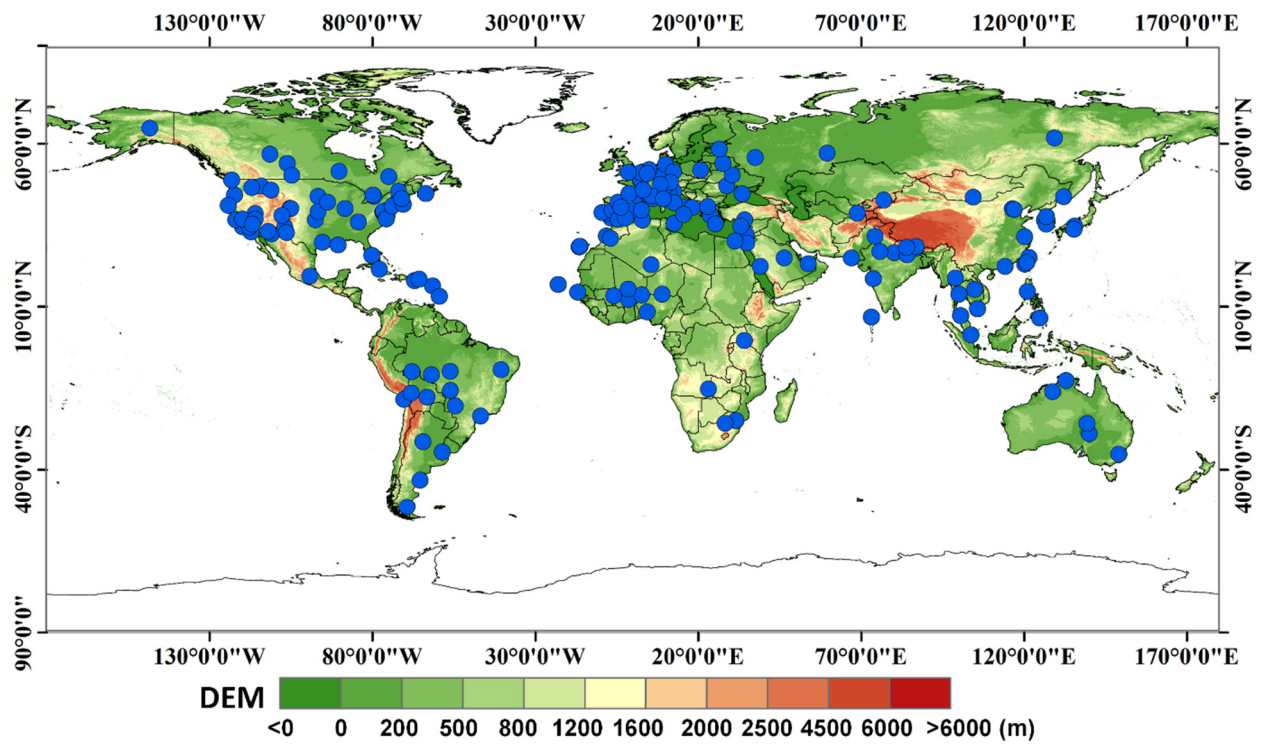
Figure S1. Map of the study area, with blue dots representing the locations of the 171 AERONET sites used. The sites provided over-land data for more than a year's observations.
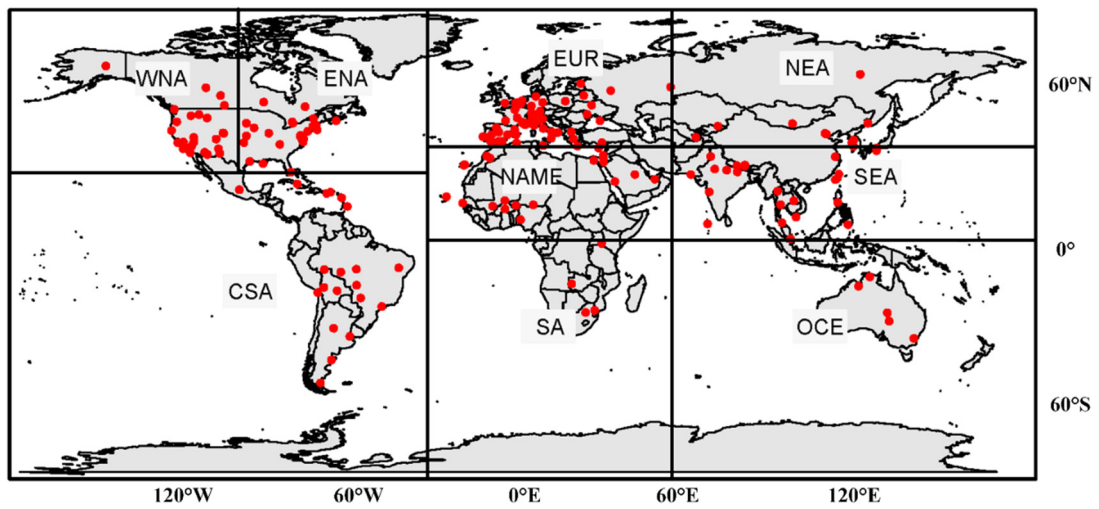
Figure S2. Geographical bounds of regions used in this study for grouping the MODIS and AERONET fAODs. The locations of AERONET sites are represented by the red dots. The names of regions and associated abbreviations are: Eastern North America (ENA), Western North America (WNA), Central/South America (CSA), Eurasia (EUR), North Africa/Middle East (NAME), Southern Africa (SA), North-East Asia (NEA), South-East Asia (SEA), and Oceania (OCE) (Sayer et al., 2014).
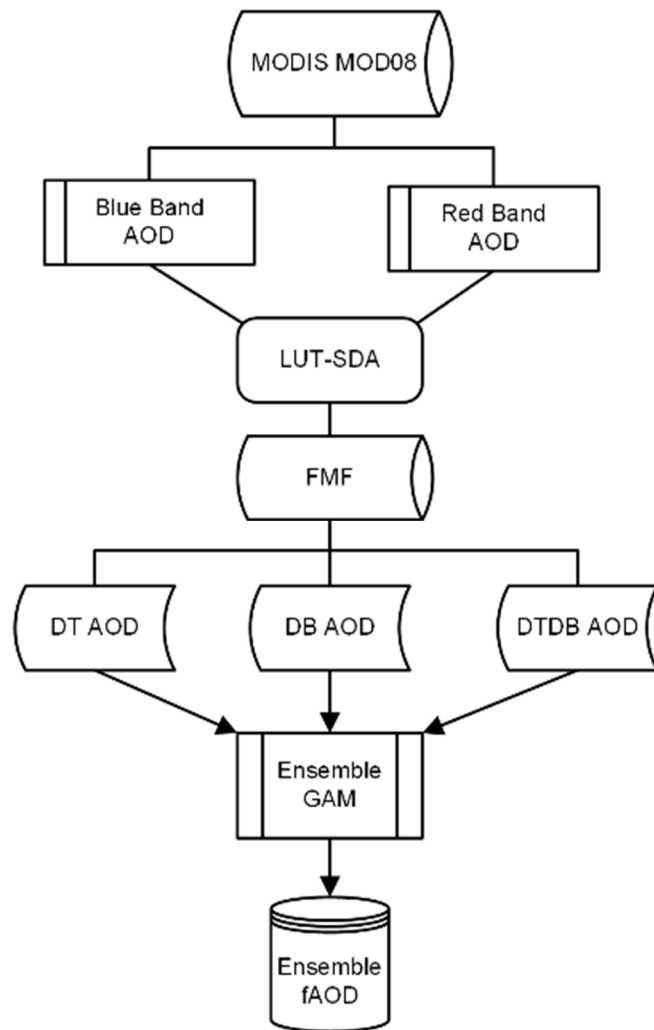
Figure S3. Schematic diagram describing the technical route for deriving the Ensemble fAOD product proposed in this study.
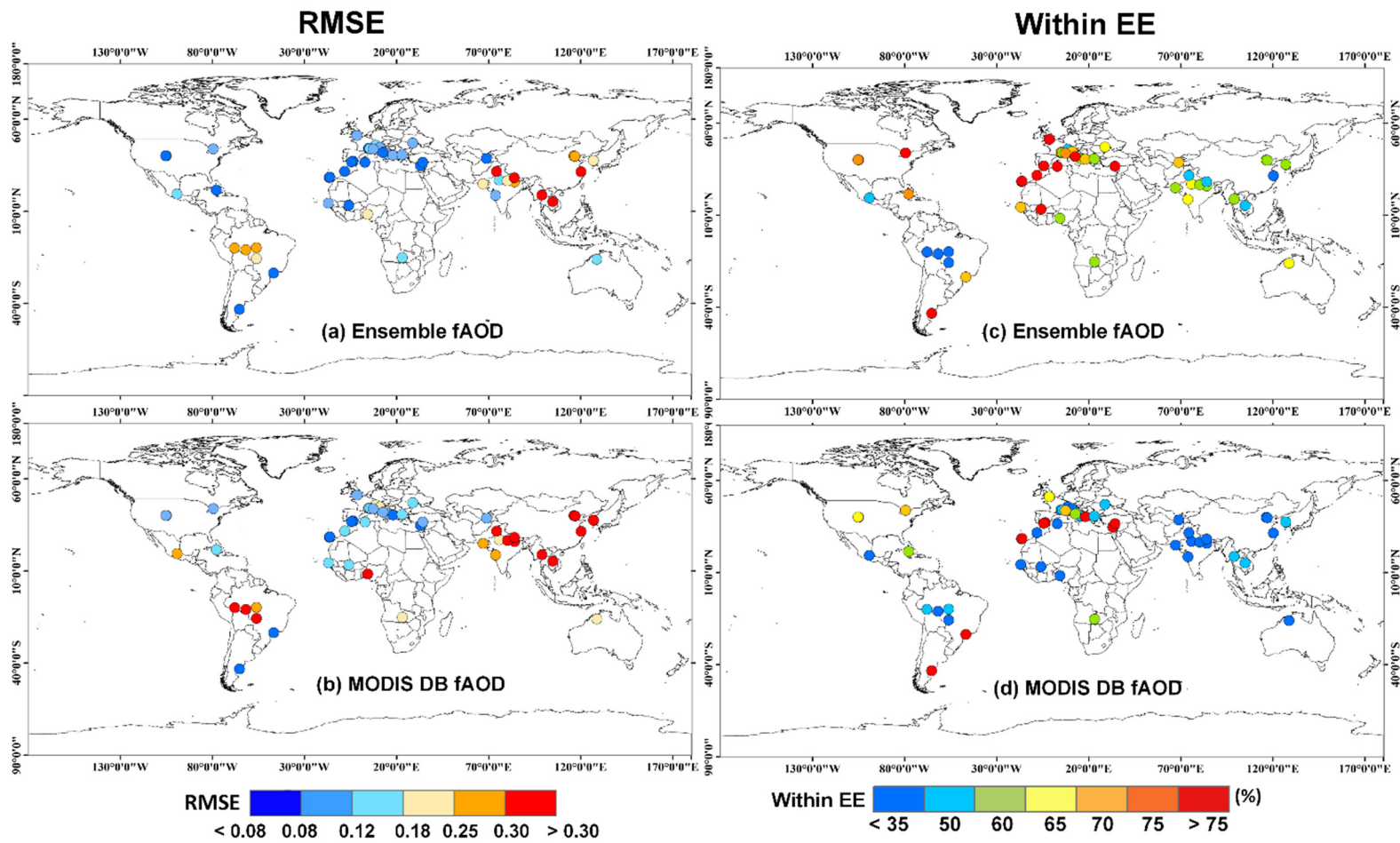
Figure S4. The RMSEs ((a) and (b)) and the percentages within the EE ((c) and (d)) for the Ensemble fAOD products and MODIS DB fAOD products.

Section S1. MODIS FMF-based fAOD spatial distribution and validation

Fig S5 shows the 9-year averaged global spatial distributions of the MODIS C6.1 Daily DT (Fig. S5(a)), DB (Fig. S5(b)), and DTDB (Fig. S5(c)) fAOD products from 2008–2016, where the spatial distribution is based on only those pixels having daily fAOD samples of over 80 days per year. The MODIS FMF-based fAODs of the three products are high in most parts of central South America (mainly the Amazon zone) and Laos. Although the general distribution characteristics for the three fAOD datasets are comparable, the values for the MODIS DB are slightly lower. Also, the DT fAODs are significantly higher than the DB fAODs in Southeast China, central Congo, and the region near the Amazon of South America, with a maximum difference of 0.25. Overall, the MODIS FMF-based fAODs are certainly inaccurate, with obvious underestimation due to many zero or close-to-zero values.
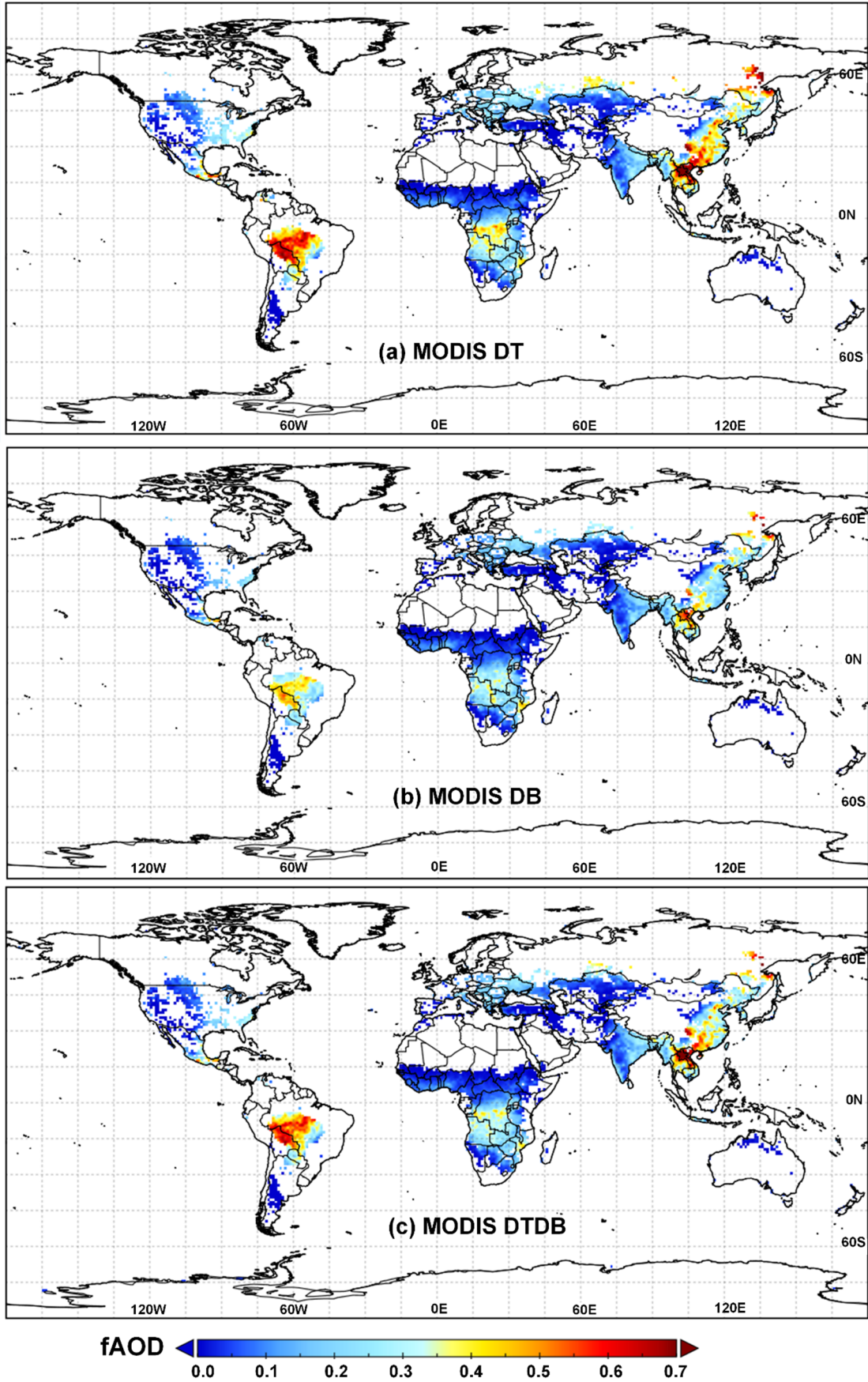
Figure S5. 9-Year average spatial distributions for the MODIS C6.1 DT, DB, DTDB, and DT-DB

fAOD products for the years 2008-2016 (the spatial distribution is based on only those pixels having daily fAOD samples of over 80 days per year).

The overall performances of the MODIS FMF-based DT, DB, and DTDB fAOD retrievals against AERONET fAOD measurements from 2008-2016 are displayed in Figure S6. We picked out 10,805 collocated matchups for the 171 available sites for all three products. All three MODIS fAOD products are somewhat correlated with AERONET ground-based fAOD measurements, with R^2 values generally around 0.30. The MODIS DB fAOD products show the highest R^2 value of 0.33. Meanwhile, the DB fAOD also yields the least MAE value (0.176) compared to 0.185 and 0.180 for the DT and DTDB products, respectively. Approximately 32.8%, 37.8%, and 35.2% of the DT, DB, and DTDB fAOD collections, respectively, fall within the EE. However, many zero or close-to-zero values are present for all three MODIS fAOD products. The main reason for this phenomenon is that the MODIS-derived FMF also contains some zero or close-to-zero values. Therefore, a significant underestimation is evident in the MODIS fAOD retrievals compared to AERONET measurements. Similar observations are reported in Jethva et al. (2010) and Yan et al. (2019).

Figure S6. Density scatterplot of MODIS C6.1: (a) DT, (b) DB, and (c) DTDB fAODs against AERONET fAOD products for 2008-2016 over land. These fAODs were derived using the MODIS C5.2 DT-based FMF according to Eq. (3). The 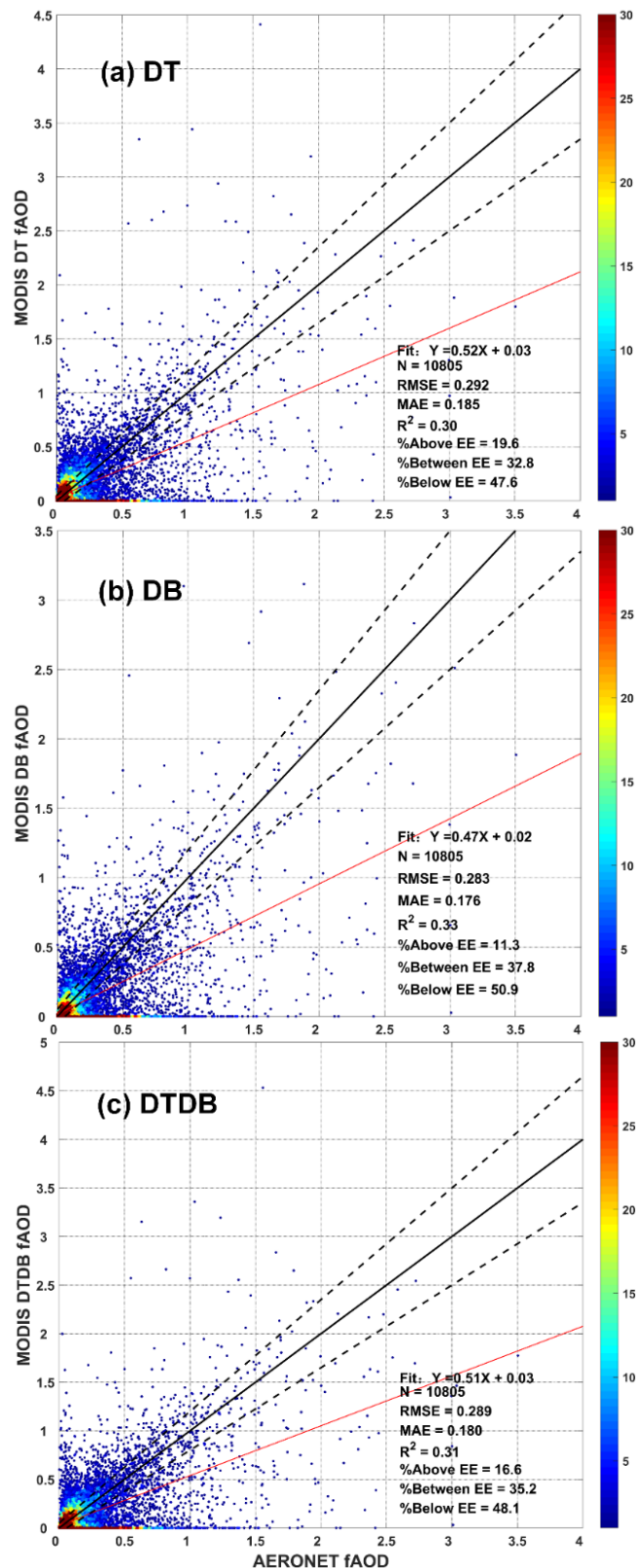dashed, black solid, and red solid lines represent the expected error range, 1:1 line, and linear regression of the scattered dots, respectively. (Comparison of AERONET fine-mode AOD (fAOD) and MODIS)

Section S2. LUT-SDA FMF-based fAOD spatial distribution and validation

Figure S7 shows the 9-year mean LUT-SDA FMF-based fAOD spatial distributions for 2008-2016, where the spatial distribution is based on only those pixels having daily fAOD samples of over 80 days per year. In general, the high value areas are mainly in southeast China and northern India, with fAOD loadings commonly exceeding 0.5. In addition, fAOD values are also relatively high in Russia, central Africa, and the Amazon region, with values of 0.2-0.3. Low fAOD loads of less than 0.1 are seen in western North America, southeastern South America, northern Europe, Australia, and southern Africa. These results are consistent Lee and Chuang (2013), although in China, our high value areas cover a relatively smaller area. However, the distributions of the LUT-SDA FMF-based DT fAODs is significantly overestimated compared to others. Especially, in central Africa, eastern America, and central Asia, the LUT-SDA FMF-based DT fAOD values are higher than those from other products by about 0.1. Moreover, compared to three other products, the distribution characteristics of the DT product in the Xinjiang Uygur Autonomous Region, China differs significantly with the incidence of fAOD values exceeding 0.5 in the region. In addition, the LUT-SDA FMF-based DT and DB fAOD products differ regarding magnitude.
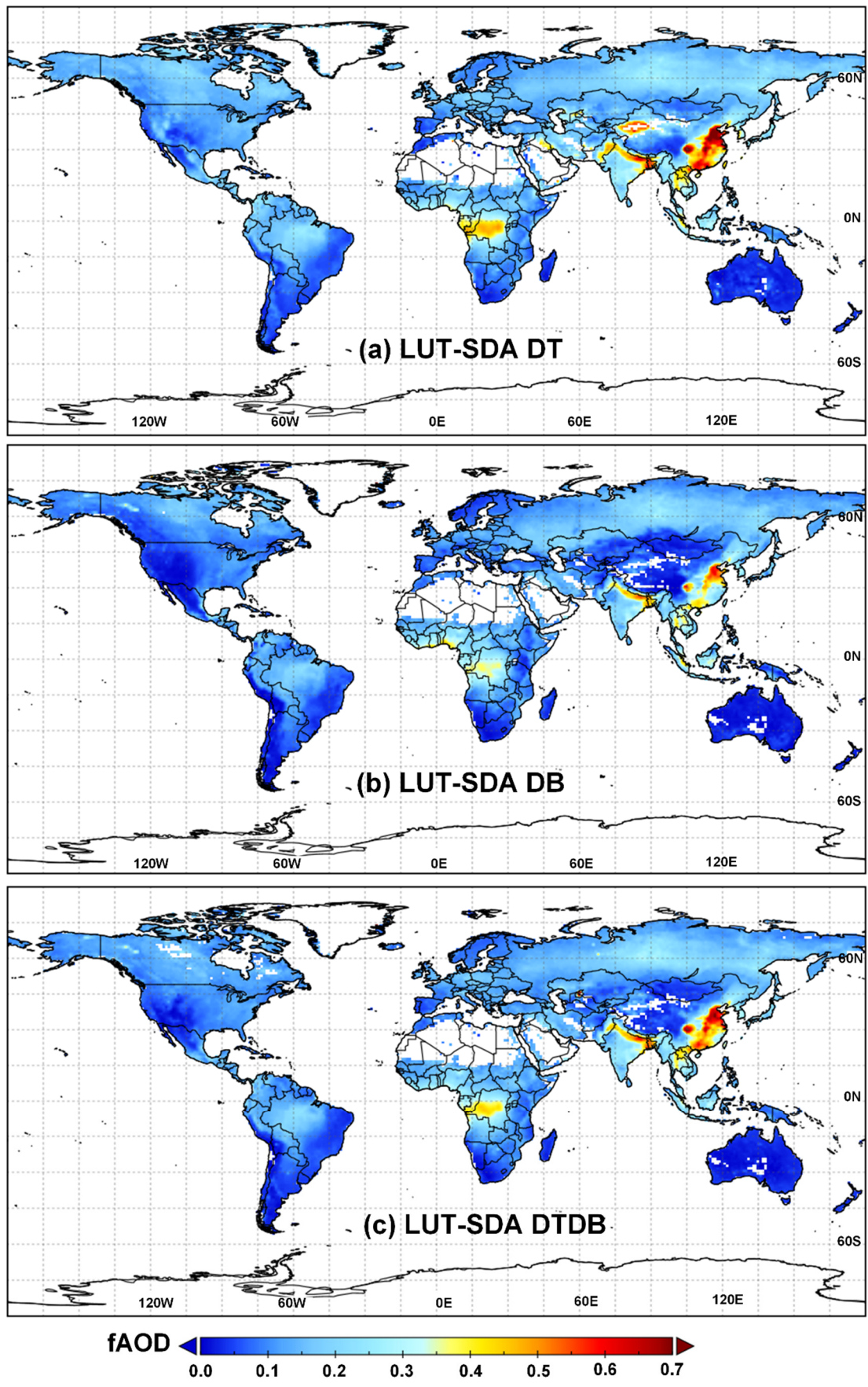
Figure S7. Global spatial distributions of the 9-year annual mean fAOD for the LUT-SDA FMF-

based fAOD (a, b, and c) products and (d) the newly merged fAOD product for 2008–2016 (the spatial distribution is based on only those pixels having daily fAOD samples of over 80 days per year).

Figure S8 displays the overall performance of the LUT-SDA FMF-based fAOD from DT, DB, and DTDB methods for 2008-2016 including all 93,172 matched samples collected from 171 AERONET sites for validation. The R^2 values of the LUT-SDA FMF-based DT, DB, and DTDB fAOD are 0.59, 0.57, and 0.61 while the RMSEs are 0.130, 0.121, and 0.119, respectively. Compared with the MODIS FMF-based fAOD, the accuracy of the LUT-SDA FMF-based fAOD significantly improves the R^2 values by 0.29, 0.24, and 0.3 while the RMSEs decreased by 0.162, 0.162, and 0.17 for the DT, DB, and DTDB fAOD products, respectively (Fig S8 (a) - (c)). Meanwhile, the percentages of the LUT-SDA FMF-based DT, DB, and DTDB fAOD falling within the EE envelope are 64%, 73.3%, and 72.4%, respectively, also highlighting major improvement. Obviously, the LUT-SDA FMF-based DTDB fAOD product exhibits the best performance for all three.

Figure S9 displays the percentages of the LUT-SDA FMF-based fAOD retrievals falling within the expected error (EE) envelopes at each AERONET site around the world. Most areas in the world show data with over 50% within the EE, especially in America, Europe, and South America, where the percentages within the EE exceed over 70%. The performances in Asia and Africa are relatively poor, with percentages within the EE hardly surpassing 60% in most areas. Similar observations are evident in Figure S10 for the RMSEs of the LUT-SDA FMF-based fAODs at each site. The RMSEs in Asia are relatively higher than those in other areas with values close to 0.2, while in America, Europe, and South America, the values are generally less than 0.1. By contrast, the LUT-SDA FMF-based DTDB fAOD product performs poorly in Asia, even poorer than the DB in southern Asia. For example, in Beijing, China, the percentage within the EE of the DB fAOD is higher than that of the DTDB in Beijing. In Taihu, China, the RMSEs of the LUT-SDA FMF-based DB fAODs are indeed lower than those of the DTDB. Therefore, by directly adopting the LUT-SDA FMF-based DTDB fAOD product, the spatial accuracy in Asia will be worse, even though the overall performance of the DTDB fAOD is the best according to Figure S8. Consequently, we used the algorithm in **Section II D** for a new fAOD ensemble, minimizing the limitation.
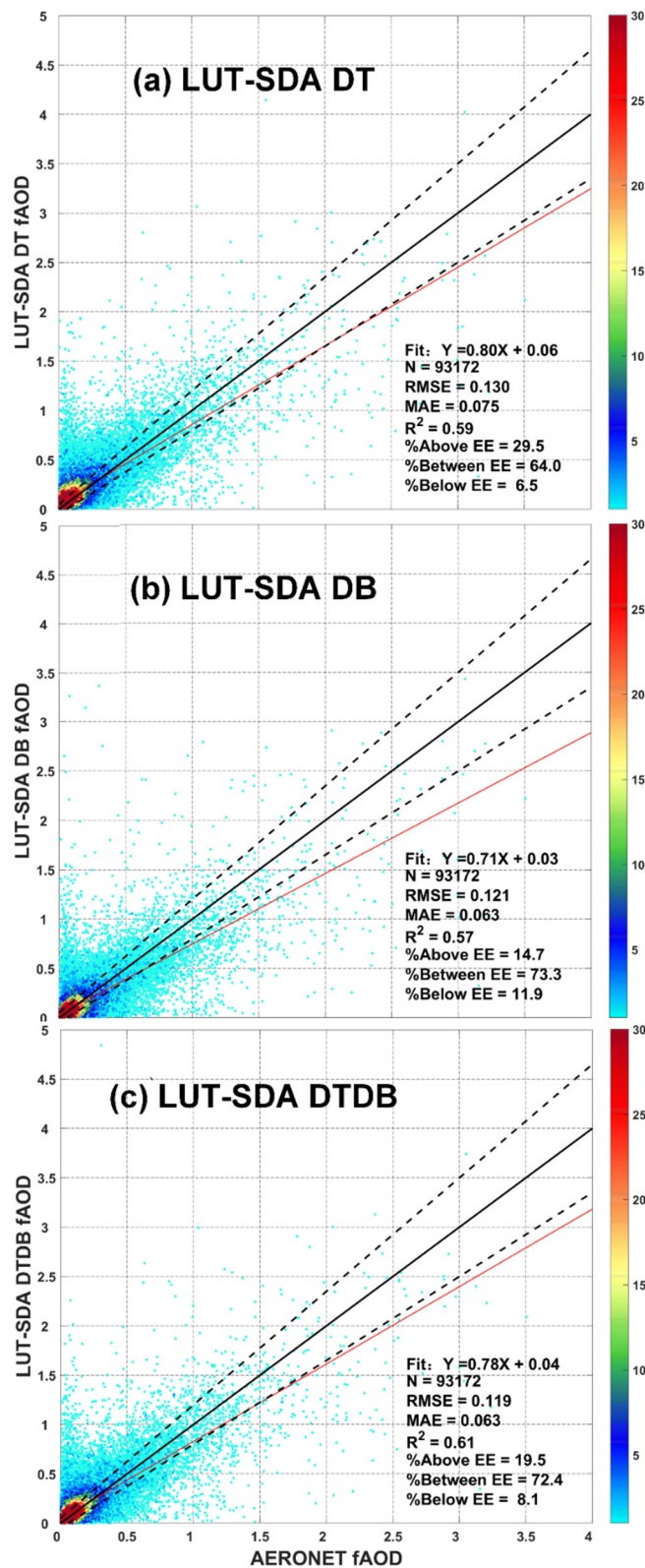
Figure S8. Improved density scatterplots of the MODIS C6.1: (a) DT, (b) DB, and (c) DTDBs fAOD over-land products after using the LUT-SDA FMF for 2008-2016 at 171 AERONET sites. The dashed, black solid, and red solid lines represent the expected error range, 1:1 line, and linear regression of the scattered dots, respectively.
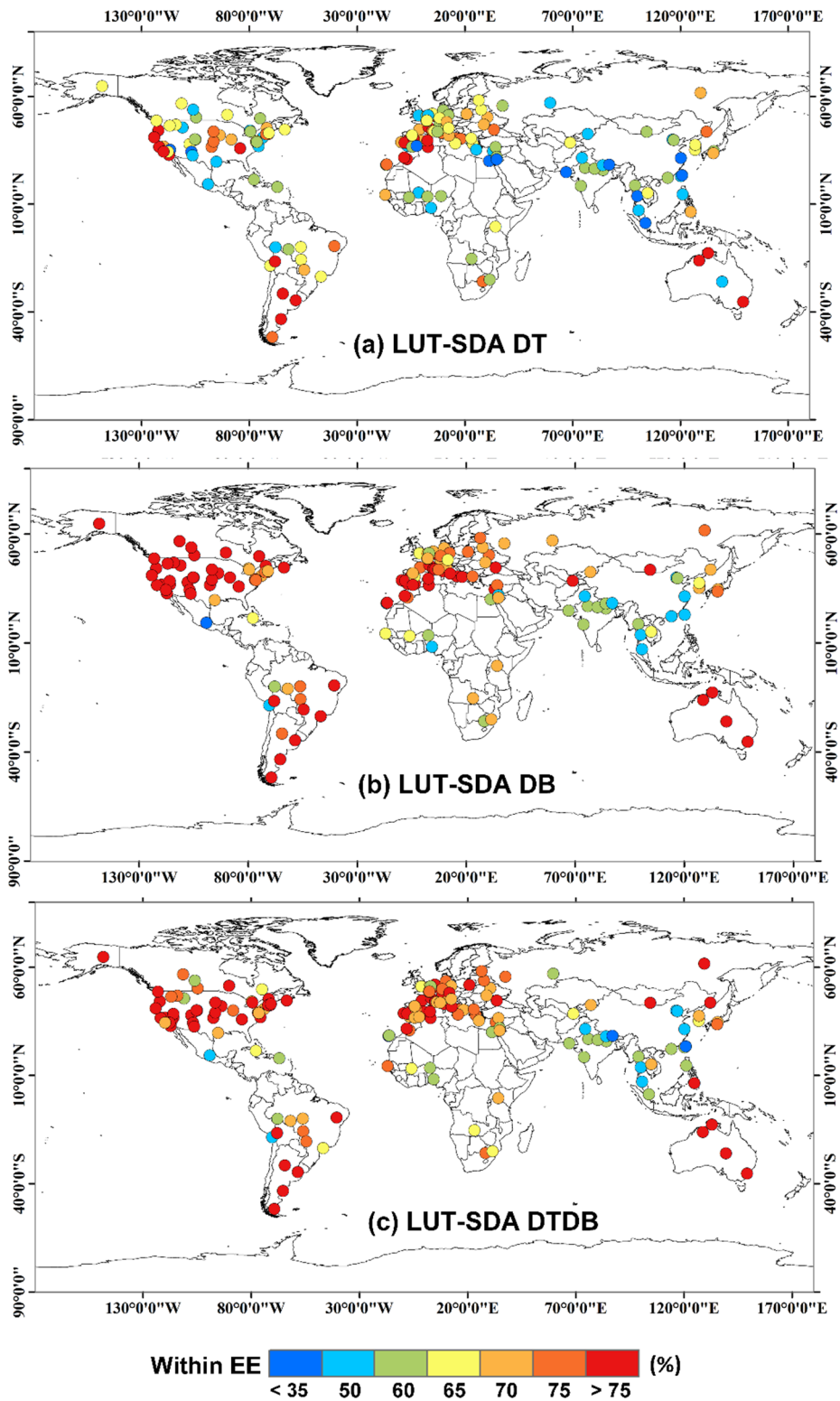
Figure S9. Percentage of fAOD retrievals within the expected error (EE) envelopes (%) for the LUT-SDA FMF-based DT, DB, DTDB, and newly merged fAOD retrievals against AERONET fAODs for each site from 2008-2016.

Figure S10. RMSEs for fAOD retrievals of the LUT-SDA FMF-based DT, DB, DTDB, and newly merged fAOD retrievals against AERONET fAODs for each site from 2008-2016.

TABLE S1. Evaluation of Ensemble fAOD at 171 AERONET sites during 2008-2016

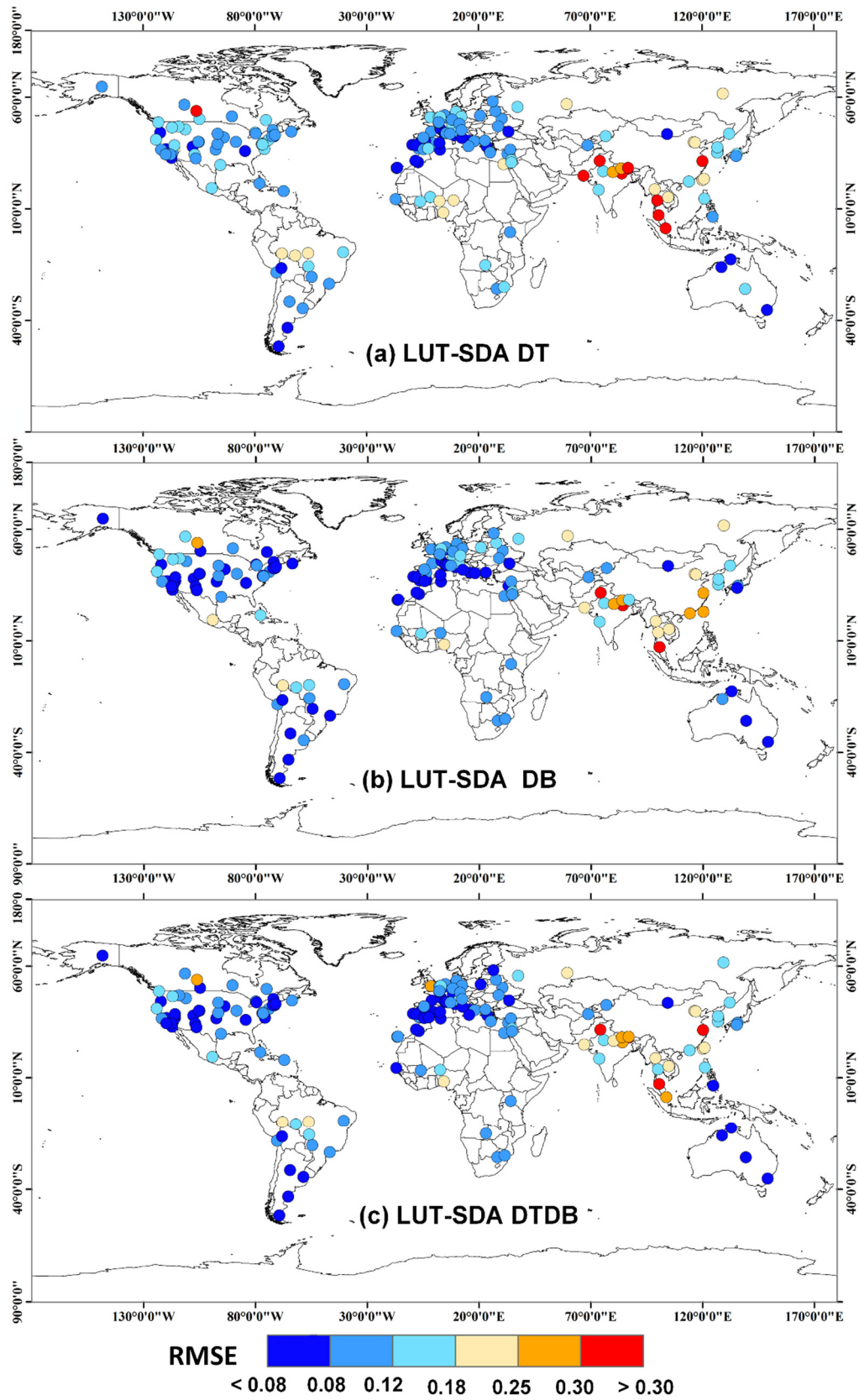| Site Name	Number of Matchups	RMSE	Between EE (%)	R	Mean Absolute Error (MAE)
ATHENS-NOA	799	0.079726	70.71339	0.248631	0.498629
Alta_Floresta	704	0.140878	71.875	0.58535	0.765082
Ames	606	0.074273	80.033	0.462429	0.680021
Arcachon	803	0.07115	78.58032	0.204526	0.452245
Arica	619	0.076217	78.02908	0.009571	0.09783
Aubiere_LAMP	576	0.047366	87.84722	0.594243	0.770872
Autilla	838	0.050564	78.75895	0.38794	0.622848
Avignon	910	0.093779	74.83516	0.221407	0.470539
BONDVILLE	611	0.09199	79.86907	0.39602	0.629301
BSRN_BAO_Boulder	1026	0.058782	86.74464	0.404271	0.635823
Banizoumbou	168	0.111372	63.09524	0.082753	0.287668
Beijing	1060	0.220373	58.86792	0.792112	0.890007
Belsk	645	0.07144	79.53488	0.475084	0.689263
Billerica	760	0.061376	80.39474	0.606825	0.77899
Birdsville	777	0.031375	93.30759	0.08857	0.297607
Blida	471	0.052891	84.71338	0.265934	0.515688
Bonanza_Creek	454	0.079123	79.29515	0.767477	0.876058
Bozeman	936	0.088663	72.32906	0.614874	0.784139
Bratts_Lake	475	0.06045	86.10526	0.446976	0.668562
Brussels	311	0.060453	81.35048	0.637484	0.798426
Burjassot	130	0.063306	81.53846	0.31471	0.56099
CARTEL	582	0.075934	77.14777	0.348623	0.590443
CCNY	1025	0.116843	67.5122	0.106083	0.325704
CEILAP-BA	1209	0.051394	84.53267	0.109909	0.331526
CEILAP-RG	318	0.04841	83.33333	3.72E-05	-0.0061
COVE_SEAPRISM	598	0.070875	80.26756	0.567779	0.753511
CUIABA-MIRANDA	1189	0.111477	74.68461	0.395827	0.629147
CUT-TEPAK	1038	0.060651	83.62235	0.290488	0.538969
Cabauw	441	0.087537	74.82993	0.322906	0.568249
Cabo_da_Roca	623	0.068265	76.40449	0.138357	0.371963
Caceres	488	0.04282	90.57377	0.252708	0.502701
Cairo_EMA_2	962	0.100163	62.16216	0.09869	0.31415
Camaguey	924	0.091282	64.50216	0.069282	0.263216
Campo_Grande_SONDA	619	0.07286	78.51373	0.230059	0.479644
Canberra	973	0.03607	93.8335	0.124221	0.352449
Carpentras	1755	0.059875	79.37322	0.518092	0.719786
Cart_Site	1247	0.060021	82.9992	0.370983	0.609084
Chapais	217	0.07383	76.95853	0.505963	0.711311
Chen-Kung_Univ	422	0.180981	53.08057	0.67071	0.818969
Chiang_Mai_Met_Sta	831	0.22733	56.79904	0.68282	0.826329
Chilbolton	357	0.129969	69.46779	0.189833	0.435698

Cordoba-CETT	210	0.050951	87.14286	0.158133	0.397659
Dakar	1165	0.069636	74.24893	0.360547	0.600456
Dalanzadgad	560	0.041506	93.03571	0.483343	0.695229
Davos	366	0.098833	52.45902	0.066594	0.258058
Dunkerque	495	0.086261	67.47475	0.344952	0.587326
Dushanbe	1134	0.082195	75.92593	0.191055	0.437099
EVK2-CNR	326	0.287362	15.33742	0.287256	0.535963
Egbert	908	0.073315	80.72687	0.534548	0.731128
El_Arenosillo	636	0.08429	66.98113	0.062575	0.25015
Ersa	1264	0.057262	78.56013	0.434129	0.658885
Evora	1137	0.050083	87.95075	0.264366	0.514166
FORTH_CRETE	946	0.088096	65.4334	0.06631	0.257507
Fort_McMurray	622	0.100894	80.22508	0.507532	0.712413
Frenchman_Flat	872	0.079222	54.70183	0.10975	0.331286
Fresno	439	0.065356	75.62642	0.413246	0.642842
GSFC	1308	0.079824	77.37003	0.665017	0.815486
Gandhi_College	757	0.286771	55.21797	0.46181	0.679566
Goldstone	778	0.029556	94.98715	0.048381	0.219956
Granada	1808	0.080895	67.97566	0.065508	0.255945
Gwangju_GIST	649	0.146923	62.86595	0.559221	0.747811
HJAndrews	207	0.048174	87.92271	0.219458	0.468463
Halifax	649	0.11582	77.9661	0.240975	0.490892
Hamburg	331	0.081317	74.92447	0.368054	0.606674
Harvard_Forest	620	0.068215	80	0.560643	0.748761
Hong_Kong_PolyU	428	0.179712	54.43925	0.630663	0.794143
ICIPE-Mbita	960	0.093093	69.79167	0.405058	0.636442
IER_Cinzana	1327	0.086501	74.15222	0.259499	0.50941
IMAA_Potenza	1324	0.073816	74.32024	0.107283	0.327541
IMS-METU-ERDEMLI	1773	0.091799	68.07671	0.280656	0.52977
Ilorin	666	0.202106	51.2012	0.374125	0.611658
Ispra	1332	0.108837	63.96396	0.329714	0.574207
Issyk-Kul	1065	0.091645	66.57277	0.054844	0.234187
Izana	1033	0.121426	34.26912	0.021205	0.145619
Jabiru	978	0.052396	86.80982	0.394047	0.627732
Jaipur	1188	0.15163	61.53199	0.539573	0.734556
Ji_Parana_SE	809	0.162299	65.14215	0.699223	0.836196
KONZA_EDC	586	0.090848	79.35154	0.196739	0.443552
Kanpur	1386	0.240444	55.19481	0.594259	0.770882
Karachi	1187	0.225665	51.22157	0.089347	0.29891
Kyiv	656	0.106071	67.9878	0.237067	0.486895
La_Jolla	307	0.047324	86.64495	0.240739	0.490651
La_Laguna	1188	0.107863	58.83838	0.020329	0.14258
La_Parguera	788	0.080389	57.1066	0.055267	0.23509
La_Paz	643	0.047658	89.11353	0.006263	0.079137

Laegeren	422	0.07914	76.06635	0.187504	0.433017
Lahore	871	0.352261	43.97245	0.251952	0.501948
Lake_Argyle	1506	0.06984	84.26295	0.436118	0.660393
Lecce_University	864	0.095949	68.1713	0.185727	0.430961
Leipzig	511	0.11627	65.55773	0.351177	0.592602
Lille	511	0.081931	73.58121	0.535158	0.731545
Lulin	138	0.195168	21.73913	0.088406	0.297331
MD_Science_Center	1011	0.090431	73.98615	0.484521	0.696075
Madrid	604	0.072674	72.68212	0.138043	0.371541
Mainz	599	0.073101	76.29382	0.276811	0.526128
Malaga	1315	0.069787	69.58175	0.140038	0.374217
Manila_Observatory	188	0.120003	59.57447	0.140549	0.374899
Mauna_Loa	184	0.108138	45.1087	0.000245	-0.01564
Messina	476	0.07814	71.63866	0.201112	0.448455
Mexico_City	569	0.157302	46.57293	0.180362	0.424691
Minsk	557	0.084286	78.27648	0.356004	0.596661
Missoula	646	0.112747	80.18576	0.473277	0.687952
Modena	1022	0.124599	66.04697	0.299619	0.547375
Moldova	930	0.090963	69.24731	0.293071	0.54136
Mongu_Inn	677	0.110533	66.32201	0.711373	0.843429
Monterey	1136	0.092189	92.07746	0.326374	0.571292
Moscow_MSU_MO	535	0.119187	71.40187	0.468144	0.68421
Munich_University	567	0.104516	78.83598	0.199118	0.446226
ND_Marbel_Univ	224	0.077822	82.58929	0.549291	0.741142
Nes_Ziona	724	0.132831	50.69061	0.099966	0.316174
OHP_OBSERVATOIRE	1498	0.077225	68.02403	0.288563	0.537181
Oostende	266	0.151884	58.27068	0.066437	0.257754
Osaka	603	0.10341	65.67164	0.40443	0.635948
Ouarzazate	522	0.047096	76.81992	0.409055	0.639574
Palaiseau	692	0.071381	76.5896	0.513472	0.71657
Palencia	1079	0.070295	73.58665	0.204958	0.452722
Palma_de_Mallorca	839	0.060568	79.02265	0.135822	0.36854
Paris	669	0.082457	77.27952	0.342057	0.584857
Petrolina_SONDA	248	0.0825	86.29032	0.032716	0.180875
Pickle_Lake	149	0.092394	84.56376	0.477173	0.690777
Pokhara	1304	0.286178	49.69325	0.336675	0.580237
Pretoria_CSIR-DPSS	1034	0.068166	80.46422	0.523827	0.723759
Pune	960	0.120188	62.1875	0.472521	0.687401
QOMS_CAS	660	0.236906	26.21212	0.000615	-0.0248
REUNION_ST_DENIS	931	0.057379	73.79162	0.117922	0.343398
Railroad_Valley	1547	0.052761	88.62314	0.173687	0.416757
Red_Mountain_Pass	966	0.045434	86.64596	0.144838	0.380576
Rimrock	823	0.105448	80.68044	0.396697	0.629839
Rio_Branco	870	0.16445	56.32184	0.297844	0.545751

Rome_Tor_Vergata	1474	0.060508	82.56445	0.275073	0.524474
SEDE_BOKER	211	0.081745	66.82464	0.204875	0.452632
SERC	1021	0.09159	67.48286	0.528752	0.727153
Saada	1711	0.044721	90.00584	0.358234	0.598526
Santa_Cruz_Tenerife	1756	0.086445	63.09795	0.153054	0.391222
Sao_Paulo	588	0.085888	61.90476	0.110514	0.332436
Saturn_Island	720	0.116785	84.72222	0.393109	0.626984
Sevastopol	871	0.059738	86.22273	0.336438	0.580032
Sevilleta	1366	0.043855	92.82577	0.130955	0.361877
Shirahama	320	0.08707	71.5625	0.697846	0.835372
Silpakorn_Univ	1013	0.169396	48.56861	0.697568	0.835205
Singapore	166	0.291024	51.20482	0.247522	0.497515
Sioux_Falls	611	0.093597	86.41571	0.729757	0.854258
Skukuza	611	0.101505	61.21113	0.160888	0.401109
Songkhla_Met_Sta	444	0.301813	46.3964	0.23069	0.480302
TABLE_MOUNTAIN_CA	1228	0.077255	80.45603	0.01791	0.133828
Tabernas_PSA-DLR	281	0.067906	69.03915	0.314217	0.560551
Table_Mountain	1186	0.059942	84.40135	0.352068	0.593353
Taihu	317	0.329326	35.01577	0.412739	0.642447
Thessaloniki	1540	0.085487	70.25974	0.323585	0.568845
Thompson_Farm	917	0.068627	75.57252	0.417957	0.646496
Toravere	520	0.068778	77.11538	0.367262	0.606022
Toronto	918	0.078465	81.80828	0.545201	0.738377
Trelew	1267	0.05716	89.66062	0.013526	0.1163
Trinidad_Head	940	0.140097	75.21277	0.156748	0.395914
UCSB	412	0.079886	65.04854	0.114796	0.338815
Ubon_Ratchathani	471	0.181061	66.02972	0.72169	0.849523
Univ_of_Houston	1121	0.081338	66.63693	0.255237	0.50521
Ussuriysk	537	0.125521	75.41899	0.541175	0.735646
Venise	1127	0.087211	68.41171	0.347807	0.589752
Villefranche	809	0.087861	68.60321	0.378182	0.614965
Walker_Branch	140	0.068973	80	0.749826	0.865925
Waskesiu	406	0.260735	72.16749	0.313877	0.560247
White_Sands_HELSTF	1417	0.044437	90.19054	0.237537	0.487378
XiangHe	1096	0.217564	61.49635	0.841397	0.917277
Yakutsk	564	0.177712	80.85106	0.57197	0.756287
Yekaterinburg	435	0.198222	65.05747	0.409185	0.639676
Yonsei_University	742	0.145178	68.59838	0.729166	0.853912

Note: Units for RMSE (Root Mean Squared Error), Between EE, R (correlation coefficient) and MAE (Mean Absolute Error) are shown in the first column below each parameter's name.

Reference

(1) Jethva, H.; Satheesh, S. K.; Srinivasan, J.; Levy, R. C., Improved retrieval of aerosol size-resolved properties from moderate resolution imaging spectroradiometer over India: Role of aerosol model and surface reflectance. *Journal of Geophysical Research: Atmospheres* **2010,** *115*, (D18).

(2) Yan, X.; Li, Z.; Luo, N.; Shi, W.; Zhao, W.; Yang, X.; Liang, C.; Zhang, F.; Cribb, M., An improved algorithm for retrieving the fine-mode fraction of aerosol optical thickness. Part 2: Application and validation in Asia. *Remote Sensing of Environment* **2019,** *222*, 90-103.

(3) Che, H.; Qi, B.; Zhao, H.; Xia, X.; Eck, T. F.; Goloub, P.; Dubovik, O.; Estelles, V.; Cuevas-Agullo, E.; Blarel, L.; Wu, Y.; Zhu, J.; Du, R.; Wang, Y.; Wang, H.; Gui, K.; Yu, J.; Zheng, Y.; Sun, T.; Chen, Q.; Shi, G.; Zhang, X., Aerosol optical properties and direct radiative forcing based on measurements from the China Aerosol Remote Sensing Network (CARSNET) in eastern China. Atmospheric Chemistry and Physics 2018, 18, (1), 405-425.

(4) Kaufman, Y. J.; Didier, T.; Olivier, B., A satellite view of aerosols in the climate system. *Nature* **2002,** *419*, (6903), 215-23.

(5) Lee, K.; Chung, C. E., Observationally-constrained estimates of global fine-mode AOD. *Atmospheric Chemistry and Physics* **2013,** *13*, (5), 2907-2921.